ELSEVIER

Flow behaviour of a modified Zr–2.5wt%Nb pressure tube alloy

R.N. Singh [a,*], S. Mukherjee [a], R. Kishore [a], B.P. Kashyap [b]

[a] *Materials Science Division, Bhabha Atomic Research Centre, Mumbai 400-085, India*
[b] *Department of Metallurgical Engineering and Materials Science, Indian Institute of Technology, Bombay, Mumbai 400-076, India*

Abstract

Anisotropy in flow behavior of cold worked and stress-relieved Zr–2.5wt%Nb pressure tube alloy was characterized by performing tensile tests in the temperature range of 298–823 K and under a constant nominal strain-rate of $\sim 3 \times 10^{-4} \, \mathrm{s}^{-1}$. Results showed that both yield and ultimate tensile strengths of this alloy decreased gradually with increasing test temperatures, with a rapid fall in strengths above a temperature of 623 K. The tensile ductility did not change appreciably up to 673 K but increased rapidly above this temperature. A strain energy model was developed to explain the occurrence of dynamic strain ageing (DSA). Analysis of the true stress–strain behavior suggested that the flow hardening or softening behavior of this alloy can be expressed in the form of a constitutive relationship comprising of a constant, work-hardening term and a term representing flow softening due to recovery.
© 2005 Elsevier B.V. All rights reserved.

1. Introduction

In pressurized heavy water reactor (PHWR) pressure tubes are used instead of pressure vessels to contain the hot pressurized coolant [1]. The hot pressurized heavy water coolant, self weight of the tube, weight of fuel bundle and irradiation produce an environment of temperature, stress, corrosion, and radiation damage for the structural materials [2]. Such an environment leads to changes in dimensions (creep and growth); in mechanical properties (increases in strength and Delayed Hydride Cracking velocity, decreases in ductility and

fracture toughness); in microstructure (globurisation of β-phase in Zr–2.5Nb alloy in particular, change in dislocation density) and chemical composition (particularly hydrogen content) of the pressure tubes [2,3]. The design of the pressure tube is based on section III of the ASME pressure vessel code, which specifies the criteria of maximum design stress on the basis of ultimate tensile strength, yield strength, creep and stress-rupture strengths at the operating temperature. For pressure tube alloys one third of the ultimate tensile strength has been found to be the limiting property.

During normal operating condition, the pressure tubes are exposed to operating temperature of ~573 K. Exposure of the coolant tube to elevated temperature under stress and neutron irradiation requires that the coolant tube material should possess high strength and adequate creep resistance throughout its life. However,

---

* Corresponding author.
  E-mail addresses: singh@mpie.de, mms@apsara.barc.ernet.in (R.N. Singh).

during a postulated loss-of-coolant accident (LOCA), in which the primary coolant fails to remove heat from the core, the temperature of the pressure tube could rise very quickly to a temperature above 1073 K [4]. PHWR design provides for quarantining of the unsafe channels while continued harnessing of power from the safe ones. The integrity of the dry and wet quarantined channels is affected by γ-heating, enhanced oxidation and oxide embrittlement [3]. The degradation in mechanical properties at such high temperatures is an important component of pressure tube safety assessment. An understanding of the flow behavior of this alloy at elevated temperature is required to predict its deformation behavior under aforementioned conditions.

In early generation PHWR, Zircaloys (zirconium alloy with Tin as primary alloying addition) were used as pressure tubes which were later replaced by the Zr–2.5Nb alloy to obtain better in-reactor performance [5–9]. The metallurgical condition of the Zr–2.5Nb tubes varies in different countries: cold worked and annealed (Russia); cold worked and stress-relieved (Canada, India); and water quenched and aged (Russia) [2]. Initially cold-worked Zr–2.5wt%Nb alloy pressure tubes were made with the same process as used to make Zircaloy-2 pressure tubes [9–11]. The fabrication routes followed by Atomic Energy of Canada Limited (AECL) for the manufacture of cold worked and stress relieved (CWSR) Zr–2.5wt%Nb pressure tubes for CANDU type reactors are shown in Fig. 1 [10,12]. There are two broad categories: conventional and modified. Fabrication steps like multiple melting under vacuum (for chemical homogenization and control of impurity content), forging (to break the cast structure) and β-treatment (to randomize the grains) are common to both the routes. In conven-

tional route an extrusion ratio of 11:1 is employed followed by cold drawing (20%). The final step of autoclaving imparts a thin, adherent and impervious surface oxide layer to improve corrosion resistance. Later on AECL developed modified routes for improved in-reactor performance of the pressure tubes [12]. In the modified route, the extrusion ratio is reduced to about 8:1 and final dimensions are obtained by increasing the amount of cold work. There are three modified routes viz. route I, II and III. In modified route I a large (40%) cold work is followed by stress-relieving at 773 K (500 °C) for 6 h. Modified route II consists of two cold working steps of ∼20% each with an intermediate annealing at 923 K (650 °C) for 0.5 h. In modified route III first extruded tubes are annealed at 973 K (700 °C) for half an hour and then, cold work is imparted, which is followed by a stress-relieving treatment at 748 K (475 °C) for 6 h. The final autoclaving treatment for the modified route is same as that for conventional route of pressure tube fabrication. Fleck et al. [12] have investigated the microstructural changes and its effect on the properties of the tubes fabricated from the conventional and modified fabrication routes (Fig. 1 [10,12]). The microstructural parameters like grain size, its aspect ratio and dislocation density depends on the fabrication route employed [12].

The fabrication route of the Indian pressure tubes, being followed at Nuclear Fuel Complex (NFC), Hyderabad, is similar, but not same, to the modified route II of Fig. 1. As can be seen from the flow chart, shown in Fig. 2(a), the amount of cold work imparted during first cold working stage of tube fabrication at NFC is larger (50–55%) compared to the modified route II (20%) followed by AECL [12]. Apart from this, at NFC cold
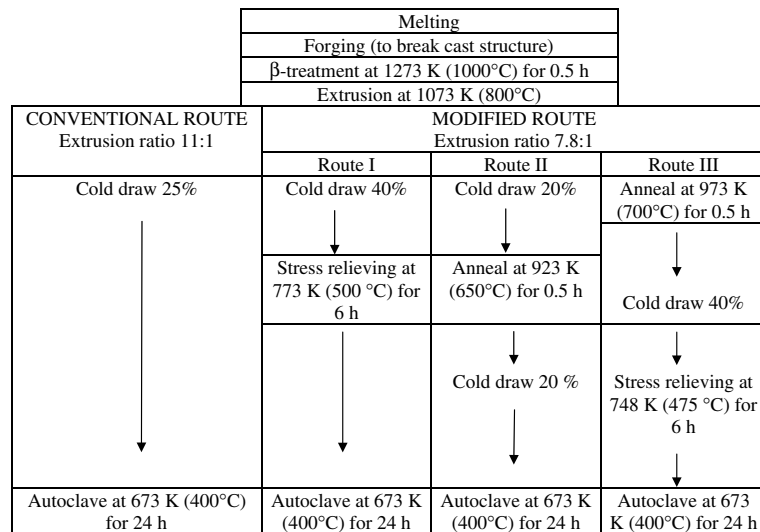
Melting			
Forging (to break cast structure)			
β-treatment at 1273 K (1000°C) for 0.5 h			
Extrusion at 1073 K (800°C)			

CONVENTIONAL ROUTE Extrusion ratio 11:1	MODIFIED ROUTE Extrusion ratio 7.8:1		
	Route I	Route II	Route III
Cold draw 25%	Cold draw 40%	Cold draw 20%	Anneal at 973 K (700°C) for 0.5 h
	Stress relieving at 773 K (500 °C) for 6 h	Anneal at 923 K (650°C) for 0.5 h	Cold draw 40%
		Cold draw 20 %	Stress relieving at 748 K (475 °C) for 6 h
Autoclave at 673 K (400°C) for 24 h	Autoclave at 673 K (400°C) for 24 h	Autoclave at 673 K (400°C) for 24 h	Autoclave at 673 K (400°C) for 24 h

Fig. 1. Production routes for the fabrication of cold-worked Zr–2.5wt%Nb tubes [10,12].

β - Quenching from 1273 K (1000 °C)/0.5h

Ingot yields three billets designated as T - top, M - middle and B - bottom

⇩

Hot Extrusion: Extrusion Ratio 8:1 (Temperature 1073K (800 °C))

⇩

Vacuum Stress relieving at 753K (480 °C)/3h

⇩

I - Pilgering 50-55 % reduction

Vacuum Annealing at 823K (550 °C)/6h

⇩

II - Pilgering 20-25 % reduction
Each billet yields two tubes

⇩

Autoclaving at 673K (400 °C)/36h

a

b
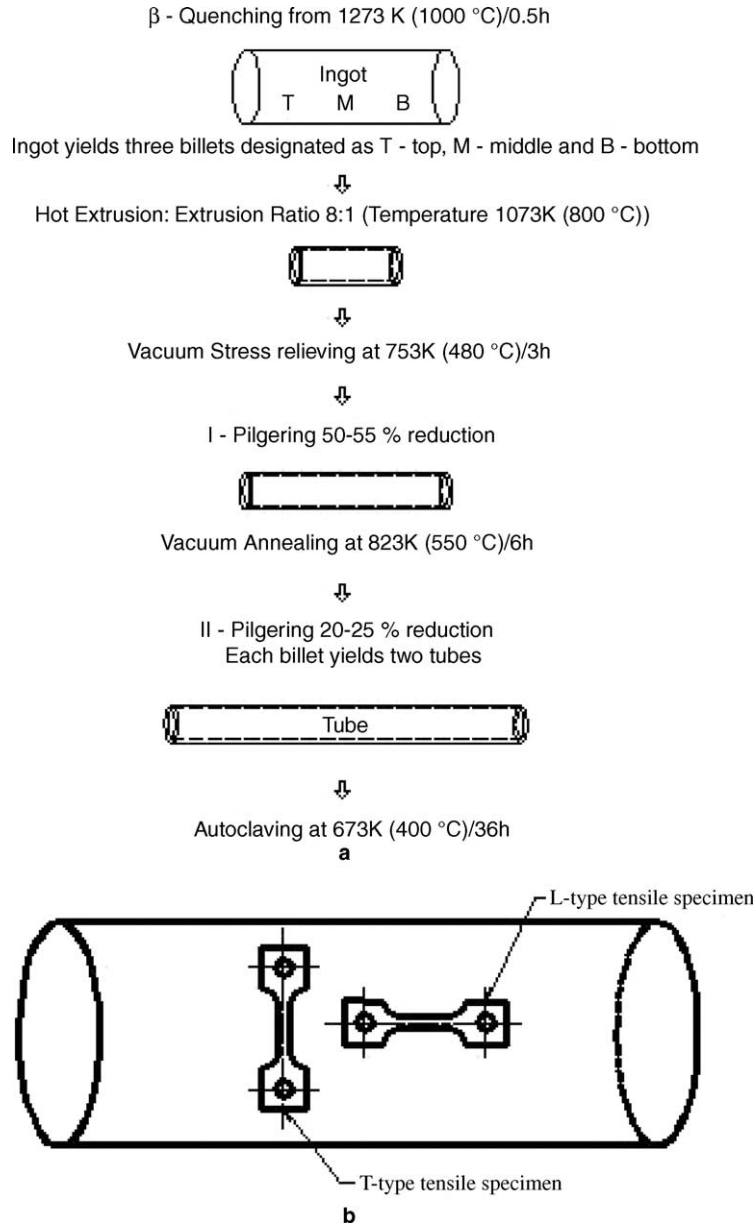
Fig. 2. (a) The modified fabrication flow sheet of Zr–2.5wt%Nb pressure tubes being followed at NFC, Hyderabad, India [13]. (b) Illustration of orientation of longitudinal (L-type) and transverse (T-type) tensile specimen with respect to pressure tube axis.

work is imparted using a process called pilgering, which imparts simultaneous reduction of wall thickness and diameter. The lower extrusion ratio employed in the modified route compared to the conventional route ensures lower aspect ratio of α-grains, less intense circumferential basal pole texture and more uniform microstructure resulting in improved irradiation resistance, reduced susceptibility to stress reorientation of hydrides, and uniform mechanical properties across the length of the tube [13].

The current fabrication route of CWSR Zr–2.5wt%Nb pressure tubes produces a two phase microstructure of strongly textured and elongated (in axial direction) α-grains surrounded by very thin nearly continuous β-phase network along the grain-boundaries [13]. The α-grains, possess HCP structure, with basal poles predominantly aligned in the circumferential (transverse) or radial direction of the tubes. Since the highly textured α-grains have limited number of slip systems, the mechanical properties of the pressure tubes are

anisotropic at ambient and reactor operating temperatures.

A literature survey [9,11,14,15] shows that the majority of the studies on the tensile properties of Zr–2.5Nb alloy are limited to the ambient and reactor operating temperature and very little information is available on the high temperature (>573 K (300 °C)) tensile properties of this material [14–17], especially for the tubes manufactured from the modified routes [14,17]. Only a few studies have so far been carried on the effects of crystallographic texture on the tensile properties of this alloy at elevated temperatures [16–20]. The objective of this investigation was to study the flow behavior of CWSR Zr–2.5wt%Nb pressure tube material as a function of test temperature and crystallographic texture. In this paper, the flow behavior of CWSR Zr–2.5wt%Nb pressure tube material manufactured by a route similar to modified route II [12] is described in terms of the stress–strain curves, tensile property dependence on temperature and specimen orientation with respect to tube axis.

2. Experimental procedure

The Zr–2.5wt%Nb pressure tube alloy was obtained from Nuclear Fuel Complex (NFC), Hyderabad, India as sections of commercial pressure tubes (103 mm internal diameter, 4.3 mm wall-thickness and 130–300 mm length). These spool pieces were taken both from finished tubes (cold worked and autoclaved) as well as from 2nd pilgered (cold worked only) tubes (Fig. 2(a)), which were manufactured from a route which was similar to modified route II (Fig. 1). Chemical analysis of these tubes indicated niobium and oxygen contents to be 2.54 wt% and 0.1175 wt%, respectively.

Sub-size sheet tensile specimens of gage length 25 mm and with their axes parallel to the longitudinal direction of the pressure tubes (L-type) were machined from sections of autoclaved tube, which were obtained from two different tubes (designated as L_1 and L_2). For machining these specimens tube sections were cut axially into three pieces each subtending an angle of 120° at the centre of the tube and the curved pieces thus obtained were cold flattened. To study the effect of crystallographic

texture on the tensile properties, both longitudinal tensile specimens (L-type) as well as transverse specimens (T-type – with specimen axis parallel to the transverse direction of the tubes) were machined from the sections of autoclaved pressure tube spools, which were cut axially into three pieces each subtending an angle of 120° at the centre of the tube and the curved pieces thus obtained were flattened in a vacuum hot press at 623 K. These specimens were designated as L_3 and T_3. Some of the tensile specimens with axis parallel to the longitudinal direction of the tube were machined from 2nd pilgered Zr–2.5Nb pressure tube spools as well (Fig. 2(a)). All the tensile specimens (L_1, L_2, L_3 and T_3) were obtained from tubes manufactured from the route (Fig. 2(a)) similar to modified route II as described in Fig. 1. The designations for both L- and T-type specimens are summarized in Table 1 and their orientations with respect to tube axis are illustrated in Fig. 2(b). The machined tensile specimens were subjected to a heat-treatment at 673 K (24 h) in an inert gas (argon) atmosphere. The tensile specimens obtained from the autoclaved material were tested in the temperature range of 298–823 K (at 50 K temperature intervals) under a nominal strain-rate of $3.3 \times 10^{-4}\,\text{s}^{-1}$. The tensile specimens obtained from the 2nd pilgered material were tested in the temperature range of 373–673 K at a temperature interval of 25 K to obtain data points at closer interval in these temperature ranges. All tension tests were conducted using an Instron make screw driven universal testing machine, fitted with a resistance heated furnace with temperature control of ±1 K. For elevated temperature tests the specimens were soaked for 1 h at the test temperature prior to the load application. During soaking and testing a continuous flow of argon gas was maintained through the furnace to minimize the oxidation of the specimens.

3. Results

3.1. Engineering stress (S)–engineering strain (e) curves

3.1.1. Autoclaved material

Typical engineering stress–strain curves for longitudinal specimens obtained from autoclaved material are

Table 1
Details of tensile specimens (TS) machined from Zr–2.5Nb pressure tubes

Tube no.	Fabrication route with respect to Fig. 1	Tube fabrication stage (Fig. 2(a))	Flattening method	TS axis orientation with respect to tube axis (Fig. 2(b))	TS designation
1	II	Autoclaved	Cold	Parallel to tube axis	L_1
2	II	Autoclaved	Cold	Parallel to tube axis	L_2
3	II	Autoclaved	Hot vacuum at 623 K	Parallel to tube axis	L_3
3	II	Autoclaved	Hot vacuum at 623 K	Perpendicular to tube axis	T_3
4	II	2nd pilgered	No flattening	Parallel to tube axis	2nd pilgered

All the specimens were subjected to a heat treatment at 673 K for 24 h.

shown in Fig. 3(a)–(c). The tensile tests were carried out in the temperature range of 298–823 K and at a constant nominal strain-rate of $3.3 \times 10^{-4}\,s^{-1}$. Fig. 3(a) shows the engineering stress–strain curves for the specimens obtained from tube L_1. The tensile curves for specimens obtained from tube L_2 are given in two separate plots for the sake of clarity (Figs. 3(b) and (c)). No serrations

could be observed on the stress–strain curves at any temperature (Fig. 3(a)–(c)). However, occasionally audible clicks were heard during plastic deformation at some temperatures. At temperatures above 623 K, the flow stress reached a peak value at smaller strains, beyond which the flow stress was observed to decrease with increasing strain (Fig. 3(c)). With increase in
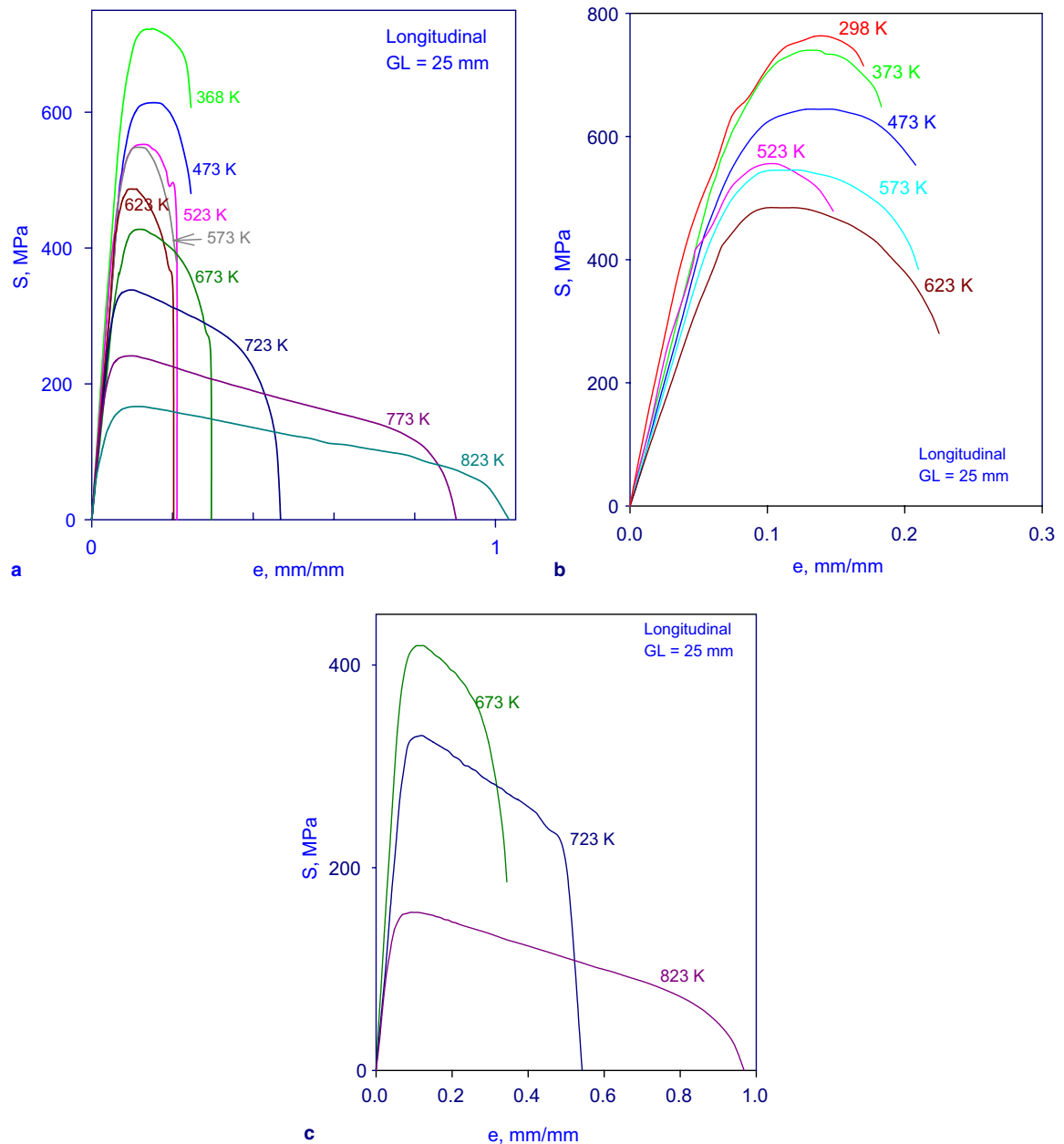
Fig. 3. Stress–strain plots for autoclaved Zr–2.5Nb pressure tube alloy at different temperature tested under a strain-rate of $3.3 \times 10^{-4}\,s^{-1}$ for longitudinal specimens (a) obtained from tube L_1 in the temperature range of 368–823 K, obtained from tube L_2 in the temperature range of (b) 298–623 K and (c) 673–823 K.

temperature, the peak flow stress and the corresponding strain decreased while the total tensile ductility increased appreciably. Similar plots for transverse specimens obtained from autoclaved material in the temperature range of 298–823 K and under identical strain-rate are shown in Fig. 4(a) and (b). The flow curves for the transverse specimens were marked by undulations and a sharp drop in engineering stress was observed after the onset of localized deformation i.e. necking (Fig. 4(a) and (b)). Comparatively, the flow curves for longitudinal specimens were smoother and the decrease in engineering stress beyond necking was gradual. For transverse specimens a sharp yield drop was also observed at temperatures of 623 and 673 K (Fig. 4(a)). At temperatures of 823 K the flow curves were observed to be marked by

few serrations coinciding with the onset of macroscopic plastic flow.

3.1.2. 2nd pilgered material

The engineering stress–strain curves of the longitudinal specimens tested at temperatures in the range 373–673 K, at a constant nominal strain-rate of $2.65 \times 10^{-4} \, s^{-1}$ are shown in Fig. 5. It may be recalled that in the temperature range of 473–623 K a minima in tensile ductility was observed for autoclaved material as well (Figs. 3(a) and (b) and 4(a)). Hence, in the aforementioned temperature range tensile tests were performed at 25 K interval. The nature of flow curves for the 2nd pilgered material was similar to that of the autoclaved material. The flow curves were smooth and no serrations were observed at any of the test temperatures. However, at some temperatures flow curves were irregular and few occasional audible clicks accompanied plastic deformation. It was noted, that at a comparable temperature, the stress–strain behavior of these specimens were very similar to those observed in the longitudinal specimens (L_1 and L_2), which were machined from the autoclaved tubes (Fig. 3(a) and (b)). Since both autoclaved and 2nd pilgered materials were not from same tube, a direct comparison of strength and ductility values were not possible.
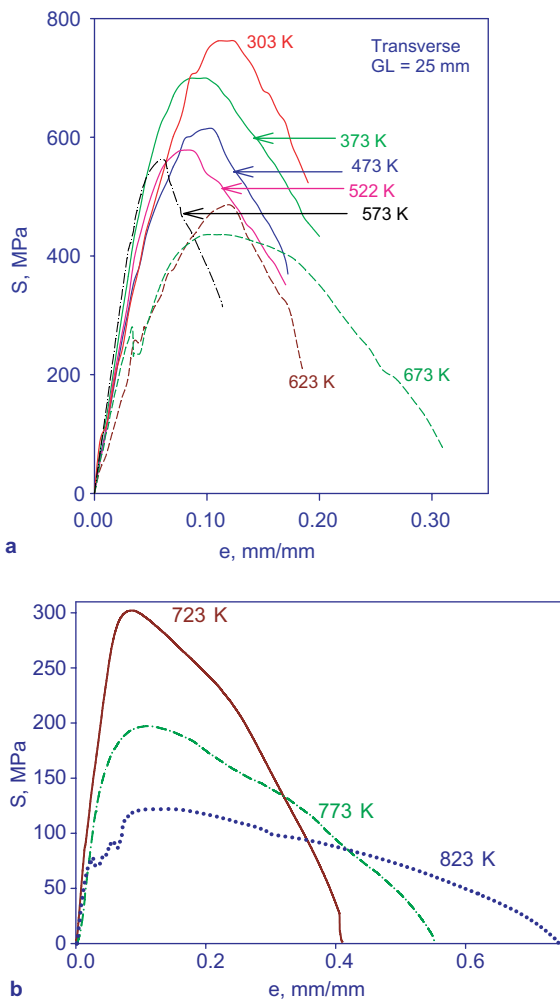

Fig. 4. Stress–strain curves for autoclaved Zr–2.5Nb pressure tube material using transverse specimens obtained from tube T_3 and tested under a strain-rate of $3.3 \times 10^{-4} \, s^{-1}$ in the temperature range of (a) 303–673 K and (b) 723–823 K.
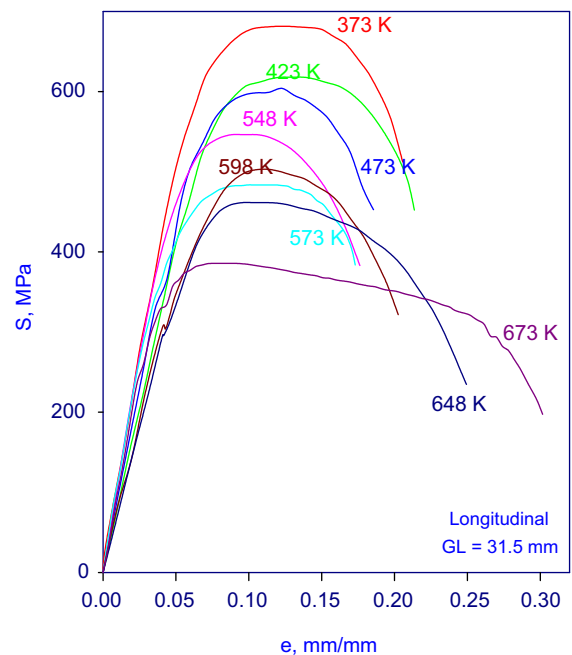

Fig. 5. Selected engineering stress–strain curves of 2nd pilgered Zr–2.5Nb pressure tube material obtained using longitudinal specimens and tested under a strain-rate of $2.65 \times 10^{-4} \, s^{-1}$ in the temperature range of 373–673 K.

3.2. Tensile properties

The variation in tensile properties viz. yield strength, ultimate tensile strength and ductility is shown in Fig. 6(a) and (b) as a function of temperature, for both longitudinal and transverse orientations of the auto-claved material. Fig. 6(a) shows tube to tube variations (L_1 and L_2) in tensile properties of the autoclaved material obtained using longitudinal specimens over the temperature range of 298–823 K. As can be seen from Fig. 6(a), both the yield and ultimate tensile strengths for the longitudinal specimens of this alloy decreased gradually with increase in temperature up to 523 K, increased marginally with increase in temperature in the temperature range of 523–573 K and thereafter the strength values decreased steeply with further increase in temperature. The total tensile elongation is practically independent of temperature up to 523 K, shows a minima in the temperature range of 523–623 K, but increases thereafter with further increase in test temperature. The tensile elongation values for tests conducted above 723 K have not been shown, as they were large compared to low temperature values. Fig. 6(b) shows the effect of orientation on tensile properties obtained
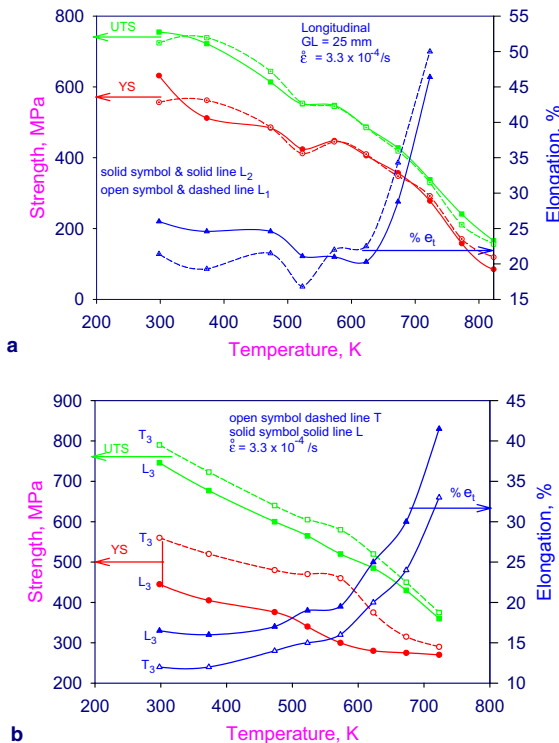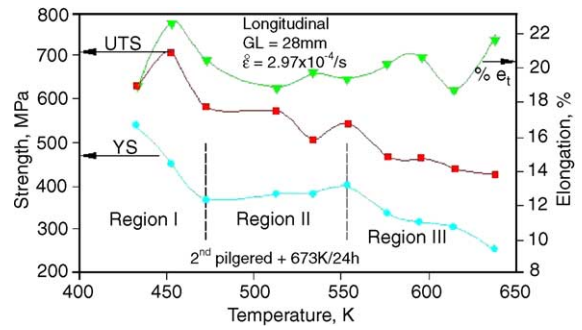

Fig. 7. Tensile properties of Zr–2.5wt%Nb pressure tube alloy (2nd pilgered + 673 K/24 h) in the temperature range of 433–633 K. The variation in tensile properties as a function of temperature suggests three regions of different characteristics.

using specimens machined from another tube (L_3 and T_3 – Table 1). The transverse specimens were noted to show consistently higher yield- and ultimate tensile strengths but lower ductility compared to longitudinal specimens up to a temperature of 823 K. The variation of the tensile properties of the 2nd pilgered material in the temperature range of 433–648 K is shown in Fig. 7. A mild increase in the yield stress but mild decrease in ultimate tensile strength and ductility with increase in test temperature was observed in the temperature range of 473–573 K. The observed results of the temperature dependence of strength and ductility (Figs. 6(a) and (b) and 7) indicated a possible occurrence of dynamic strain-aging in this alloy in the temperature range of 473–573 K.

3.3. True stress (σ)–true plastic strain (ε_{pl}) curves

Fig. 8 shows the $\sigma - \varepsilon_{pl}$ curves for the longitudinal specimens obtained from autoclaved Zr–2.5wt%Nb pressure tube material in the temperature range of 298–673 K. True stress–true strain data for Fig. 8 were obtained by analyzing the engineering stress–strain data of Fig. 3(b) and (c). True plastic strain values were calculated only for the uniform strains and data beyond localized deformation i.e. necking were ignored. At 298 K flow stress increases with increase in plastic strain showing pronounced work-hardening. As the test temperature increases the increase in the flow stress is observed only at smaller plastic strains. At higher temperatures, with increasing plastic strain the flow stress showed a tendency for saturation. In general, the flow stress was observed to decrease with increase in test temperature. Also, evident in this figure is the decrease in work-hardenability with increase in test temperature. Maximum true uniform plastic strain, ε_{pl}^{max}, was also observed to decrease with increase in test temperature up to 623 K, after which it was observed to increase rapidly with further increase in test temperature. These features

Fig. 6. Temperature dependence of tensile properties of auto-claved Zr–2.5wt%Nb pressure tube material determined using (a) L-type specimens obtained from two different tubes and (b) L- and T-type specimens machined from same tube.
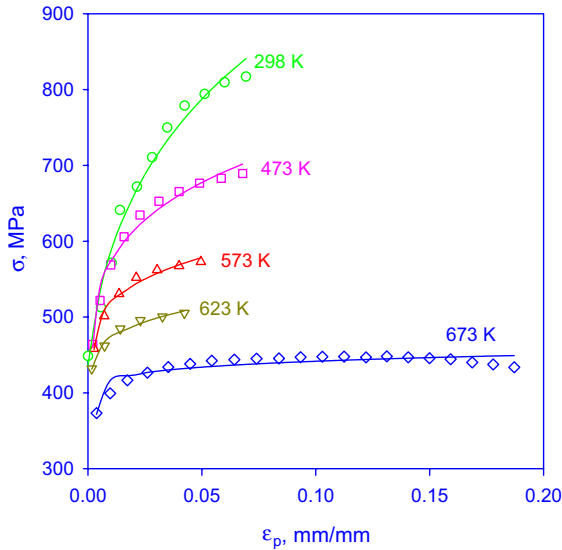
Fig. 8. True stress–true plastic strain curves (cross-plotted from Fig. 3(b) and (c)) for autoclaved Zr–2.5wt%Nb pressure tube material in the temperature range of 298–673 K obtained using longitudinal specimens.

of diminishing work-hardenability and variation in ε_{pl}^{max} with increase in test temperature are brought out more clearly in Fig. 9. The work-hardenability is defined in Eq. (1), where the σ values were taken corresponding to true plastic strains of 0.04 and 0.01.

$$\theta = \frac{\sigma_1 - \sigma_2}{\varepsilon_1^{pl} - \varepsilon_2^{pl}}. \qquad (1)$$

The $\sigma - \varepsilon_{pl}$ plots for the transverse specimens are shown in Fig. 10(a) and (b). ε_{pl}^{max} (maximum value of ε_{pl} shown in these plots) was observed to decrease with increase in test temperature before showing an increas-
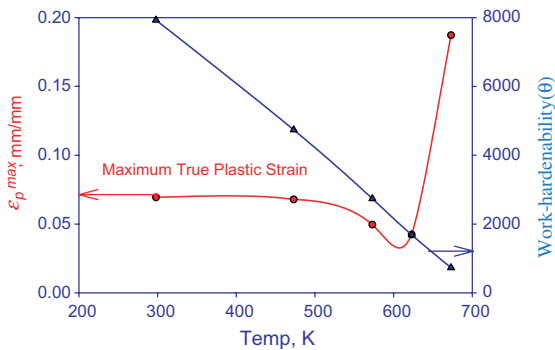
Fig. 9. The variation in maximum true plastic strain and work-hardenability with test temperature (cross-plotted from Fig. 8) for autoclaved Zr–2.5wt%Nb pressure tube material for longitudinal specimens in the temperature range of 298–673 K.
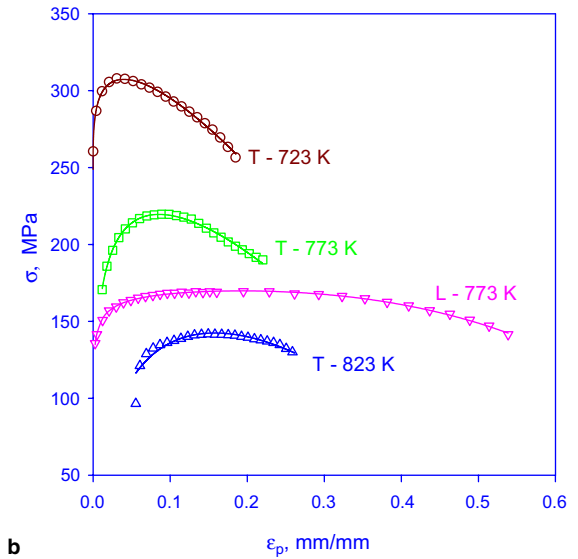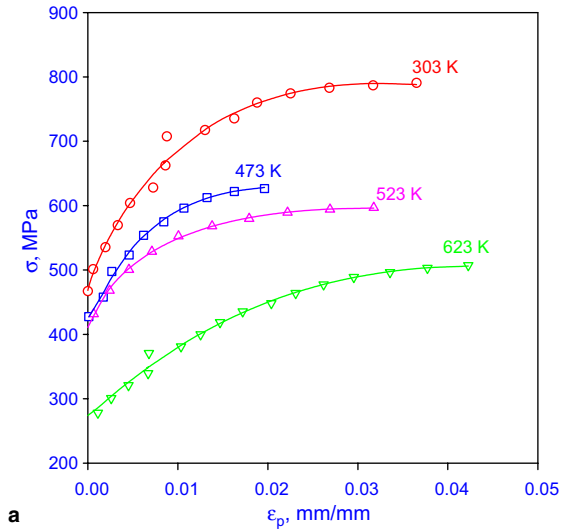

Fig. 10. (a) True stress–true plastic strain curves (cross-plotted from Fig. 4(a)) for autoclaved Zr–2.5Nb pressure tube material for transverse specimens in the temperature range of 303–623 K. (b) True stress–true plastic strain curves (cross-plotted from Figs. 3(c) and 4(b)) for autoclaved Zr–2.5wt%Nb pressure tube material in the temperature range of 723–823 K. (L and T indicate the tensile specimen orientation).

ing trend with further increase in test temperature. In the temperature range of 303–623 K, for the transverse specimens also work-hardenability diminishes with increase in test temperature. The work-hardening rate is maximum at smaller strain and saturates at larger strains. However, degree of work-hardenability is lower for the transverse specimens (Fig. 10(a)) as compared to the longitudinal ones (Fig. 8). Above 673 K, beyond a critical plastic strain, flow-softening (decrease in flow

stress with increase in plastic strain) was observed for both the orientations. The flow softening behaviour was more pronounced for the transverse specimens as compared to the longitudinal ones. The degree of flow softening, measured using an expression similar to that used for determining the degree of work-hardening (Eq. (1)), was observed to decrease with increase in test temperature.

The $\sigma - \varepsilon_{pl}$ plots (cross-plotted from Fig. 5), for the 2nd pilgered material in the temperature range of 373–673 K, is shown in Fig. 11. The nature of these plots is similar to that observed for the autoclaved longitudinal specimens. However, analysis of these plots suggested that the work-hardenability (as defined in Eq. (1)) determined corresponding to true plastic strains of 0.01 and 0.05 was independent of test temperature up to ∼548 K. In the temperature range of 548–648 K, the work-hardenability was observed to increase to a peak value before showing a decreasing trend with increase in test temperature. Maximum true uniform plastic strain was observed to decrease marginally with increasing temperature up to 648 K and thereafter showing an increasing trend with increase in test temperature. These features have been brought out more clearly in Fig. 12.

4. Discussion

The main features of the flow behaviour of the Zr–2.5wt%Nb pressure tube alloy in the temperature range of 298–823 K were: decrease in flow stress and work-hardenability with increase in test temperature; higher flow stress and lower tensile ductility for transverse orientation as compared to the longitudinal orientation; a marginal decrease in tensile elongation with increase in temperature up to a test temperature of 673 K; flow softening observed at temperatures above 673 K. All these features are discussed below.

In the temperature range from room temperature to about 773 K, α-zirconium deforms by slip primarily on the $\{10\bar{1}0\}$ first order prism planes along $\langle 1\bar{2}10 \rangle$ direction [21,22]. Slip has also been reported to occur on basal plane (0001) along $\langle 11\bar{2}0 \rangle$ direction. It has been suggested that for α-Zr prismatic slip is favoured over the basal slip in view of the lower stacking fault energy (SFE) associated with prism planes compared to other slip planes [22]. However, incidence of basal slip has been found to increase with increasing temperature, despite the predominance of $\{10\bar{1}0\}$ $\langle 11\bar{2}0 \rangle$ slip system [23]. Thus, a decrease in flow stress with increase in test temperature is due to availability of more number of slip systems with increase in test temperature.

When compared with the tensile test results of the longitudinal specimens (L₃), obtained from the same tube and under identical specimen fabrication and test condition (same temperature and strain-rate), it was observed that the T₃ specimens showed higher strength but lower work-hardenability, as compared to those of L₃ specimens, at all test temperatures between 298–623 K. It may be recalled that CWSR Zr–2.5wt%Nb pressure tube material possess a duplex microstructure of elongated, hcp α-phase grains (∼90% volume fraction [13]) and a nearly continuous grain-boundary network of bcc β-phase [12,13]. Typical α-grains dimensions are 15–30 μm along axial, 2–4 μm along circumferential and 0.2–0.4 μm along radial direction [13]. The α-grains are highly textured with ∼54% of basal poles along circumferential direction, ∼43% basal poles along radial direction and less than ∼3% along axial direction
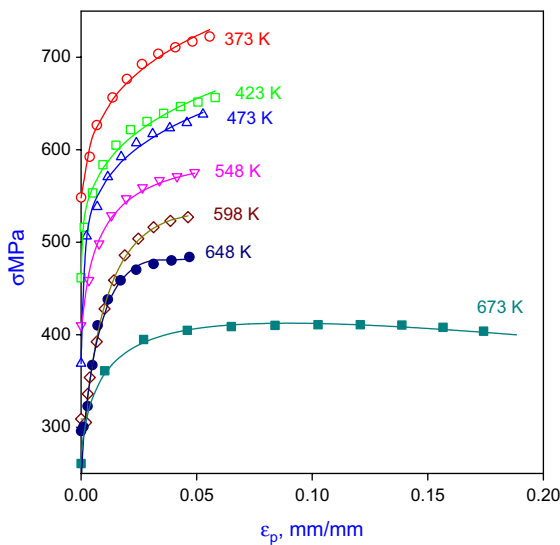

Fig. 11. True stress–true plastic strain curves of 2nd pilgered Zr–2.5wt%Nb pressure tube material for Longitudinal specimens in the temperature range of 373–673 K.
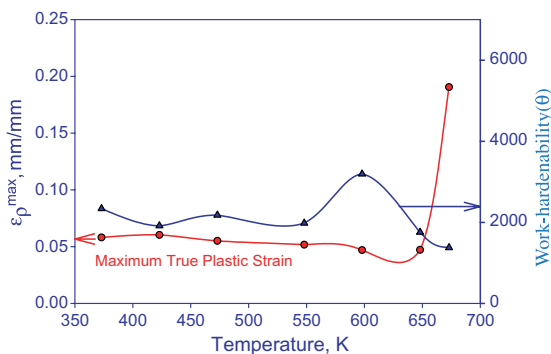

Fig. 12. Variation in work-hardenability (θ) and the maximum uniform plastic strain (cross-plotted from Fig. 11) in the temperature range of 373–673 K.

[13,24]. Since prismatic planes are the primary slip systems in α-Zr crystals, for longitudinal specimens the Schmid's factor calculated based on idealized basal pole orientation [25] given above works out to be $\cos(30°)\cos(60°) = \frac{\sqrt{3}}{4}$ for the grains having their basal poles oriented either along the circumferential or along the radial direction of the tube. For the α-Zr grains having their basal poles oriented along radial direction, for the transverse specimen also same value of Schmid's factor will be obtained. However, for the transverse specimens the Schmid's factor for the α-Zr grains having their basal poles oriented along the circumferential direction works out to be zero, as the slip vector, slip plane normal and the specimen axis are orthogonal to each other. Thus for longitudinal specimens ∼97% of the grains are likely to deform by prismatic slip whereas for transverse specimens only 43% of the grains are likely to deform by prismatic slip. As a result of this transverse orientation is harder compared to the longitudinal orientation and thereby exhibiting higher flow stress for the former. With majority of α-Zr grains not participating in plastic deformation for transverse specimens, the stress concentration at the unfavourably oriented grains will be large resulting in lower tensile ductility [26]. With increase in temperature the probability of basal slip increases which facilitates deformation of α-Zr grains having their basal poles oriented along circumferential direction [23]. Above 623 K, there practically was no difference in the strength and the work-hardenability of the two types of the specimens suggesting a weakening influence of crystallographic texture on the tensile properties of this alloy at temperatures exceeding 623 K. Above 623 K, the slopes of the stress–strain curves of both L_3 and T_3 specimens became negative after the maximum stress was reached indicating the pronounced effects of the dynamic recovery on the deformation process as reported by Shewfelt [16].

It is well known that elevated temperature flow behavior of some of the ferrous and non-ferrous alloys exhibits jerky or serrated flow, a peak in flow stress and work-hardenability, reduction in tensile ductility and negative strain-rate sensitivity of the flow stress in certain temperature and strain-rate range(s) [27–29]. This behavior is attributed to Portevin–Le–Chatelier effect [30] which occurs because of interaction of dislocation with interstitial or substitutional atmosphere or precipitates [27–29]. In some other class of alloys though the flow curves are not marked by serrations, a plateau in flow stress and work-hardenability and positive but reduced strain-rate sensitivity is observed in certain temperature ranges. This is attributed to occurrence of dynamic strain ageing (DSA). All of these macroscopic effects caused by DSA may not be very distinct in many alloys [31,32]. In the present investigation the autoclaved material showed a plateau in ultimate tensile strength (UTS) variation with temperature in the temperature

range of 523–573 K (Fig. 6(a)) but the work-hardenability value was observed to decrease with increase in temperature (Fig. 9). On the other hand in the aforementioned temperature range for 2nd pilgered material, yield strength was observed to marginally increase with increase in temperature, ultimate tensile strength was practically independent of temperature and work-hardenability showed a peak value (Figs. 7 and 12). Therefore, it becomes somewhat difficult to interpret the DSA phenomena in conventional way. In Section 4.1, a DSA model based on strain energy concept is proposed which can be used to identify the occurrence of DSA even when the macroscopic manifestations listed above are not very prominent. This model is based on the widely accepted mechanism of dislocation–solute atom interaction [27,28].

4.1. Development of elastic strain energy model of DSA

Area under the nominal stress–strain curve is a measure of the work done in deforming a material. The work done can be divided into three parts: free strain energy, locked strain energy and energy loss. As a material is worked upon, e.g. deformed in tension, initially the free strain energy increases in the material. Any further mechanical energy input to the system can be accommodated either as an increase in free strain energy or as an increase in both free and locked strain energy. Free strain energy is mechanical analogue of thermodynamic free energy whereas the locked strain energy is similar to internal energy, which in this case is energy stored/locked in and around defects. The third term could be energy loss in the form of heat, sound, etc. Thus, mathematically, we can say that the total work done in deforming a material is given by:

$$U_{total} = U_{free} + U_{locked} + U_{loss}. \tag{2}$$

4.1.1. Determination of U_{free}

From the stress–strain plot, free strain energy at a given stress (or strain) can be determined by using the relationship:

$$U_{free} = \frac{1}{2}\frac{S^2}{Slope} = \frac{1}{2}(Slope)(e_{el})^2, \tag{3}$$

where S is the engineering stress, e_{el} is the elastic strain and slope of the linear portion of the stress–strain plot is to be used. U_{free} is stored not only in the material but in the entire load train assembly (consisting of tie rod, grips, pins, load cell coupling, etc.) and the machine column. That is why the slope of the linear portion of the stress–strain curve should be taken for calculation of U_{free}, as this slope could be the measure of the combined stiffness of the specimen and the machine. The procedure to determine U_{free} has been illustrated in Fig. 13.
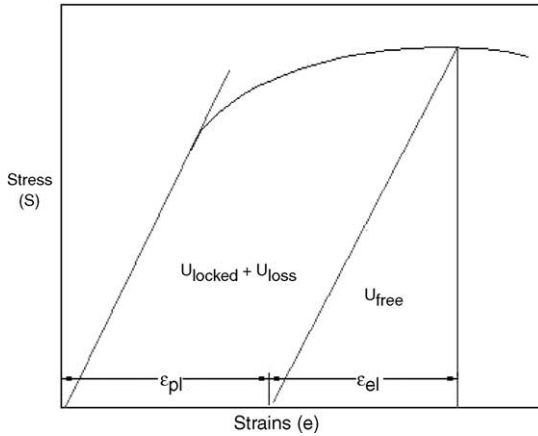
Fig. 13. Procedure to determine the free elastic strain energy from engineering stress (S)–strain (e) plot.

4.1.2. Deformation and obstacles to dislocation motion

The elastic deformation in a material under stress is caused by change in interatomic spacing. However, the interatomic bond energy is substantially reduced in the vicinity of dislocations [33], and the deformation caused by mobile dislocation motion towards the obstacles contributes to elastic deformation. In the unstressed state each mobile dislocation will have an equilibrium separation from the obstacle. The role of stress is to bring the mobile dislocations closer to the obstacle. When the stress is removed, the mobile dislocations will go back to the equilibrium separation if the obstacle was not surmounted by the applied stress. Based on free strain energy and the interaction energy of an obstacle with the mobile dislocation, the obstacles can be classified into surmountable and insurmountable obstacles. Surmountable obstacles are those, which can be surmounted under the combined action of applied stress and thermal energy while the insurmountable obstacles are those, which cannot be surmounted. Plastic deformation is caused when surmountable obstacles are overcome by dislocations. These surmountable and insurmountable obstacles are, respectively, similar to the short range and long-range obstacles [34].

4.1.3. Components of U_{free}

The reason for calling the U_{free}, free strain energy, is due to the fact that it is instantly available. Free strain energy is released on removal of load or is consumed in creating new surfaces. Changes in U_{free} is caused by increase in the potential energy of the system due to change in interatomic spacing (U_{inter}), energy required to overcome the interaction energy between mobile dislocation and surmountable obstacle (U_{sur}) and interaction energy between the mobile dislocation and insurmountable obstacle (U_{insur}). Thus we can write:

$$U_{free} = U_{inter} + U_{sur} + U_{insur}. \tag{4}$$

4.1.4. Temperature dependence of U_{free}

The temperature dependence of the free strain energy, U_{free}, will be governed by the temperature dependence of the terms on right hand side of Eq. (4). Young's modulus can be taken as the measure of the interatomic bond strength. The decrease in Young's modulus of the metallic systems with increasing temperature is gradual, with a small change per 100 K rise in temperature [35]. Hence, the first term of the Eq. (4), U_{inter} should decrease monotonically with rise in temperature. The interaction energy between mobile dislocation and insurmountable obstacle will also be a function of elastic constant and displacement function associated with the obstacle. Thus, the third term of Eq. (4), U_{insur}, should also decrease with increasing temperature.

The surmountable obstacle could be either interstitial or substitutional atoms or fine second phase precipitates. Depending on the temperature and strain-rate imposed the distribution of the solutes in alloys could be homogeneous or inhomogeneous [27]. The concentration of such solutes at/around the core of the dislocation ($C_\perp$) is higher compared to other locations (C_0). As immobile dislocations are unlikely to see any change in solute concentration it is logical to assume that the solute concentration around mobile dislocation may depend whether it is static or moving. Thus the interaction between the mobile dislocation and the surmountable obstacles will be of two types: static and dynamic. The static interaction term represents the interaction energy of the mobile dislocations with solutes corresponding to solute concentration away from core of mobile dislocation (i.e. C_0) and is a function of temperature only (for fixed material composition is constant). The dynamic interaction between the mobile dislocation and the surmountable obstacle will be a function of the instantaneous solute concentration at/around the core of dislocation (mobile dislocations either in motion or waiting in front of a surmountable obstacle), $C_\perp^i$, which in turn is decided by the temperature and strain-rate imposed. This temperature and strain-rate dependence of the solute concentration in or around dislocation core is manifested in the form of anelastic behavior.

It is proposed that the mechanism of DSA to occur is by dislocation surmountable obstacle interaction. The role of both temperature and strain-rate is to change $C_\perp^i$. Thus,

$$U_{sur} = U_{static}(C_0) + U_{dynamic}\left(\frac{C_\perp^i}{C_0}\right). \tag{5}$$

For a fully annealed microstructure the first term of Eq. (5) should be independent of strain-rate and weakly dependent on temperature and should decrease with rise in temperature. Assuming a relationship similar to the one proposed by Cottrell [36] for the interaction energy

between the solute concentration at dislocation core and dislocation, we can write:

$$U_{\text{dynamic}} = \sum_{j=1}^{k} \alpha_j RT \ln \left(\frac{{}^j C_{\perp}^i}{C_0} \right),$$ (6)

where α_j is the conversion cum scaling factor for microscopic interaction energy (energy per mole) to macroscopic strain energy (energy per unit volume). The summation should be carried out for all possible (say k) types of interaction. The term U_{dynamic} is required to overcome the combined macroscopic manifestation of the microscopic phenomena like size factor and modulus interaction of solutes with all types of mobile dislocations. This includes interactions not only due to the solute drag theory proposed by Cottrell [37] but also due to the solutes catching up with the mobile dislocations waiting in front of an obstacle [38]. At very low temperatures and high strain-rates, because of lower diffusivity even though inhomogeneous distribution of solutes will exist, kinetics will restrict the value of instantaneous solute concentration at mobile dislocation core, $C_{\perp}^i$, comparable to that of C_0. For $C_{\perp}^i = C_0$, U_{dynamic} should be zero (from Eq. (6)). As the solute concentration increases the interaction energy should also increase. Ultimately at some value of $C_{\perp}^i$, mobile dislocation will get saturated with solutes and thus saturation value of the dynamic interaction energy will be reached. On the other hand, at very high temperatures and lower strain-rates, there will be uniform distribution of solutes and $C_{\perp}^i$ will be equal to C_0 and hence U_{dynamic} will be negligible. Hence it is logical to assume that U_{dynamic} is a function of $C_{\perp}^i$. Van Den Beukel [39] has shown that the solute concentration at the waiting dislocation is a function of strain, strain-rate and Temperature. The same line of argument will hold true for the solute concentration at the moving dislocation. Thus, in general,

$$C_{\perp}^i = C_{\perp}^i(\varepsilon, \dot{\varepsilon}, T).$$ (7)

Thus, the temperature and strain-rate dependence of the second term of Eq. (5) comes through $C_{\perp}^i$. Depending upon the appropriate combination of strain-rate and temperature $C_{\perp}^i$ will show a maximum and hence U_{dynamic} will also show a maxima leading to a hump in U_{free} versus temperature plot. Fig. 14 shows the schematic variation of the components of free strain energy, U_{free} with temperature. Thus the strain-rate and temperature regime which will show a maxima in the U_{free} versus temperature plot will correspond to DSA regime.

4.1.5. U_{free} and tensile ductility

Usually the temperature and strain-rate regimes in which an alloy is susceptible to DSA, a reduction in tensile ductility is also observed. The reason for the reduced ductility during DSA is attributed to reduction in resistance to necking because of negative or reduced strain-
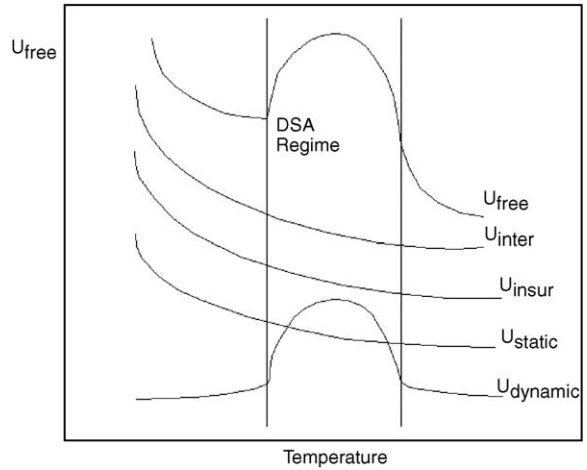

Fig. 14. Schematics showing the variation of the components of free elastic strain energy, U_{free} with temperature.

rate sensitivity. However, reduction in tensile ductility can also be explained in terms of the free strain energy parameter. There are two critical values of U_{free}, one corresponding to the initiation of macroscopic plastic flow (analogous to yield strength) and the other corresponding to the creation of new surface (analogous to ultimate tensile strength) i.e. initiation of fracture in material. The energy required to create a new surface (fracture) is supplied mainly by U_{free}. However, ${}^{\text{local}}U_{\text{locked}}$, (local relaxation of U_{locked} within a few grain thickness from the fracture surface) will also contribute marginally to the creation of new surface. Thus, a material parameter, called critical strain energy for fracture, ${}^0 U_{\text{fracture}}$, can be defined as ${}^0 U_{\text{fracture}} = U_{\text{free}} + {}^{\text{local}}U_{\text{locked}}$. As the plastic strain in the material increases the local contribution of the U_{locked} is also likely to increase. In such a case ${}^\varepsilon U_{\text{fracture}}$ (U_{fracture} at a given strain ε) $= {}^0 U_{\text{fracture}} - {}^{\text{local}}U_{\text{locked}}$, and hence will decrease with strain. The variation in ${}^\varepsilon U_{\text{fracture}}$ with strain has been shown in the schematics of Fig. 15. Based on the above argument, ${}^\varepsilon U_{\text{fracture}}$ has been shown to decrease marginally with increasing strain. The decrease may be linear or non-linear depending on the variation of ${}^{\text{local}}U_{\text{locked}}$ with
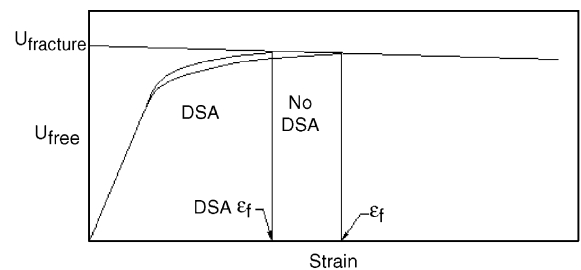

Fig. 15. The variation of critical fracture strain energy, U_{fracture}, with strain.

strain. The fracture in a material component gets initiated when the free strain energy, U_{free} is equal to $^\varepsilon U_{fracture}$. As shown in Fig. 15, in the DSA regime, U_{free} reaches the $^\varepsilon U_{fracture}$ at a smaller strain and thereby reducing the total tensile ductility.

4.2. DSA model and deformation behavior of Zr–2.5Nb alloy

The occurrence of DSA has been reported in reactor grade zirconium [40]. Also, studies on elevated temperature deformation behavior of Zr–2.5Nb alloy by the present author [17,41] revealed a plateau and peak region of yield strength and work-hardening at 523–573 K, indicating the possible occurrence of DSA at these temperatures. However, the temperature dependence of tensile strength and ductility did not show a large change (Figs. 6 and 7). Hence, the free strain energy parameter, maximum value of U_{free} (corresponding to UTS), was determined and its variation with temperature has also been shown in Fig. 16 (cross-plotted from Fig. 3(a)). The variation in the maximum value of U_{free} obtained from the data of Fig. 3(b) and (c) is shown in Fig. 17. Additionally, in Fig. 17 the value of U_{free} corresponding to a constant strain of 10.8% is also plotted as a function of test temperature.

It can be seen from Figs. 16 and 17 that the value of U_{free} decreases with rise in test temperature up to 523 K. However, in the temperature range of 523–623 K, U_{free} first increases and then falls with further rise in test temperature. The point to be noted here is that the small
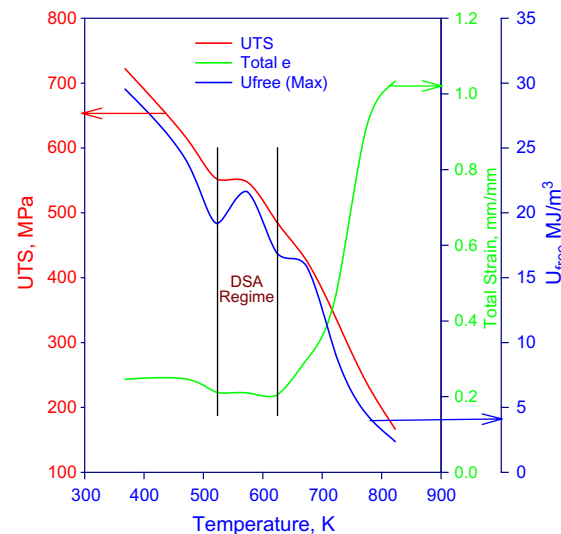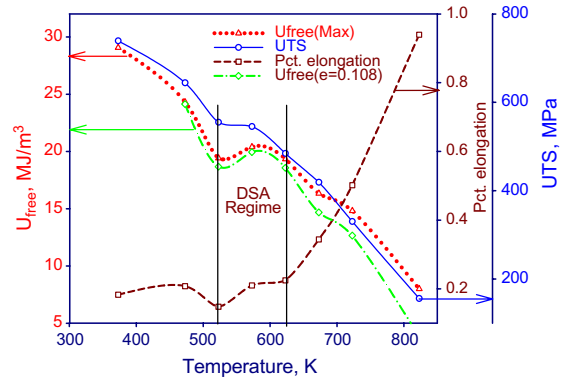

Fig. 17. Variation of ultimate tensile strength (UTS), total tensile strain and free elastic strain energy, U_{free}, with temperature for autoclaved Zr–2.5wt%Nb pressure tube material in the temperature range of 298–823 K for longitudinal specimens (cross-plotted from Fig. 3(b) and (c)).

plateau observed in the UTS versus temperature plot corresponds exactly with the hump in U_{free} versus temperature plot. Beyond this temperature, the free elastic strain energy decreases with further rise in test temperature. Thus, the variation in U_{free} is as per the prediction of our model. Based on the variation in the U_{free} values and the ductility values the temperature range susceptible to the DSA is also indicated in Figs. 16 and 17. The marginal decrease in tensile ductility can also be understood in terms of the increased free strain energy. The free strain energy is responsible for the creation of new surface i.e. fracture. In the DSA regime the critical fracture strain energy is attained at a lower strain and thereby reducing tensile ductility (Fig. 15).

4.3. Modelling of flow behaviour

The understanding of the flow behaviour of Zr–2.5Nb pressure tube alloy is of great importance to predict the deformation behaviour of the pressure tubes under LOCA condition. As was reported in Section 3.3 the flow behaviour of this alloy is marked by work-hardening at ambient temperature. With increase in test temperature the work-hardenability decreases and above 623 K the flow curves exhibited flow softening due to recovery. Four empirical equations have been extensively used to describe the work-hardening behaviour of metals and alloys [41–44]. Various parameters corresponding to the four equations obtained from the non-linear regression analysis using the stress–strain data obtained from tensile specimen machined from 2nd pilgered Zr–2.5Nb pressure tube material with the specimen axis along longitudinal direction and tested at the temperature of 548 K (275 °C) are shown below along with the regression coefficients:

Fig. 16. Variation of ultimate tensile strength (UTS), total tensile strain and free elastic strain energy, U_{free}, with temperature for autoclaved materials (cross-plotted from Fig. 3(a)).

Holloman's relation [41]

$$\sigma = 1.127 \times 10^3 \varepsilon_t^{0.288} \quad (r^2 = 87.01\%). \tag{8}$$

Ludwik's relation [42]

$$\sigma = -2.93 \times 10^3 + 3.68 \times 10^3 \varepsilon_{pl}^{0.015} \quad (r^2 = 96.2\%). \tag{9}$$

Swift's relation [43]

$$\sigma = 781.7(4.17 \times 10^{-11} + \varepsilon)^{0.101} \quad (r^2 = 94.7\%). \tag{10}$$

Voce's relation [44]

$$\sigma = 575.3 - (575.3 - 365.9)e^{-94.17\varepsilon} \quad (r^2 = 99.8\%). \tag{11}$$

As can be inferred from Eqs. (8)–(11), the work-hardening behavior of this alloy is described reasonably well with regression coefficients greater than 90%. The analysis of the stress–strain curves obtained from both L and T type specimens machined from the autoclaved material was also performed and the regression coefficient values greater than 90% were obtained suggesting that both Eqs. (10) and (11) represent the work-hardening behavior of this alloy reasonably well. However, these equations do not represent the flow softening behavior and hence cannot be used to predict the flow behavior under postulated LOCA condition.

The temperature dependence of flow stress of the metals and alloys exhibiting flow hardening and flow softening can be represented in the form of a constitutive relationship comprising of three terms: a constant term representing yield stress, a term representing work-hardening term and an exponential term representing recovery. In the present analysis the first two terms were similar to the expression for the Ludwik relation given in Eq. (9). Zhou and Clode [45] have suggested a constitutive relationship to describe the flow softening due to competing hardening and recovery processes and heat generation during plastic deformation. At lower strain-rate, as was the case in the present investigation, flow softening due to heat generation will be insignificant. The flow softening due to recovery was suggested to be dependent on peak stress and an exponential function of true plastic strain [45]. In the present analysis also, a similar expression was used. Thus, the general form of the constitutive relationship for uniaxial tension test at constant temperature and strain-rate is given in Eq. (12).

$$\sigma = \sigma_0 + k_1(\varepsilon_{pl})^n - \sigma_p \exp(-k_2(\varepsilon_{pl})^r), \tag{12}$$

where σ_p is the peak stress, σ_0, k_1, k_2, n and r are fitting parameters.

The values of the fitting parameters of the Eq. (12) were obtained using a non-linear regression analysis of the experimental data. The predicted values of the flow stress obtained using the fitting parameters of Eq. (12) are shown as solid lines in Figs. 8, 10(a) and (b) and 11. As is evident from these figures the experimentally

observed flow stress values and the values predicted using Eq. (12) is very close to each other. The temperature dependence of σ_0 and k_1, n, k_2, and r for L_2 and T_3 type specimens obtained from autoclaved material is shown in Figs. 18–21, respectively. The temperature dependence of σ_0 was similar to that of the yield stress of the material (Fig. 6(a)) and was observed to decrease with increase in test temperature (Fig. 18). The decrease in σ_0 value became more pronounced as the test temperature increased. For both L_2 and T_3 type specimens the temperature dependence of the σ_0 could be represented by a cubic polynomial equation. The temperature dependence of k_1 is also shown in Fig. 18 for both L_2 and T_3 type specimens and was also observed to decrease with increase in test temperature. Though the k_1 values showed nearly constant temperature dependence for L_2
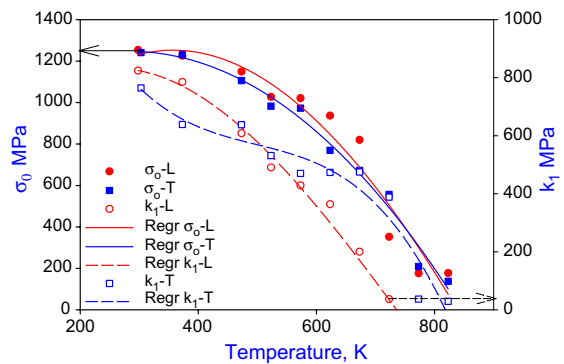
Fig. 18. Variation in σ_0 (solid symbols) and k_1 (open symbols) with temperature for longitudinal (circle) and transverse (square) specimens.
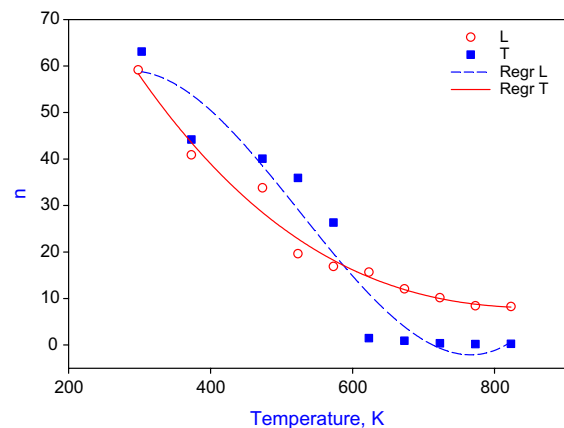
Fig. 19. Variation in n with temperature for longitudinal (circle) and transverse (square) specimens. The lines represent cubic polynomial fit.
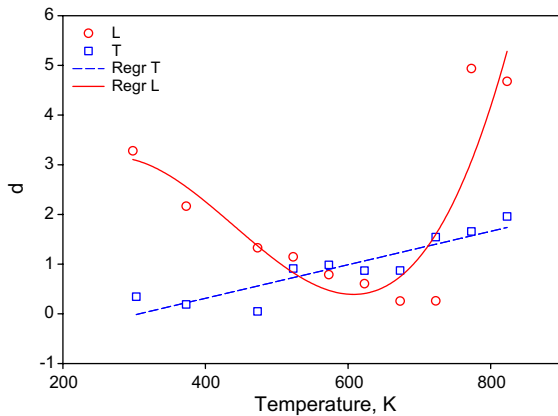
Fig. 20. Variation in k_2 with temperature for longitudinal (circle) and transverse (square) specimens. The lines represent cubic polynomial fit for longitudinal and linear fit for transverse specimens.
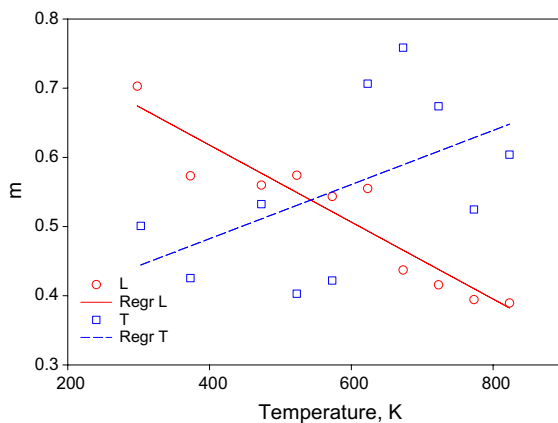

Fig. 21. Variation in r with temperature for longitudinal (circle) and transverse (square) specimens. As can be seen large scatter were observed to suggest any meaningful temperature dependence. The lines represent linear fit.

type specimens in the entire test temperature regime, for T_3 type specimens the temperature dependence was weak below 623 K and much stronger above this temperature. The parameter n which can be thought to represent the work-hardening exponent was also observed to decrease with increase in temperature (Fig. 19). The n values decreased sharply at lower temperatures and showed weak temperature dependence at higher temperatures. All the three parameters σ_0, k_1 and n were observed to decrease with increase in temperature and can be associated with physical significance in terms of the dislocation theory of plastic deformation. An increase in test temperature reduces these parameters as thermally activated cross-slip and climb of dislocation

become easy at higher temperature. Also, with activation of new slip systems at higher temperature more grains can participate in plastic deformation thereby reducing the geometrical constraints imposed by the grains not participating in deformation. The third term of Eq. (12) represents flow softening due to recovery and is important to obtain a close fit with experimental data. The predicted flow stress values were observed to be very sensitive to k_2. But the variation in fitting parameters k_2, and r (Figs. 20 and 21, respectively) representing the recovery term were neither internally consistent nor showing any meaningful trend and hence it was not possible to attach any physical meaning to these parameters.

5. Conclusions

Flow behavior of the Zr–2.5Nb pressure tube alloy manufactured from a modified route was examined in the temperature range of 298–823 K. For specimens, obtained from a given tube, transverse specimens of Zr–2.5Nb alloy possessed higher strengths and lower ductility as compared to those of longitudinal specimens up to a temperature of 623 K. Above this temperature, the tensile properties of both the types of specimens became almost comparable, indicating a strong influence of texture on tensile properties up to about 623 K. Tube to tube variations affect the mechanical properties appreciably and care should be exercised in comparing the anisotropic effect for specimens obtained from different tubes. Free elastic strain energy parameter proposed in this work can be used as a criterion for determining the susceptibility to DSA of this alloy. The flow behavior of this alloy can be represented in terms of a constitutive relationship comprising of three terms viz., a constant, a term representing increase in flow stress due to work-hardening and a term representing decrease in stress due to recovery in the entire temperature range of 298–823 K.

References

[1] S. Glasstone, A. Sesonske, Nuclear Reactor Engineering, 3rd Ed., CBS Publishers and Distributors, Delhi (India), 1988, p. 740.

[2] 'Overview' in: A.M. Garde, E.R. Bradley (Eds.), Zirconium in the Nuclear Industry: Tenth International Symposium, ASTM STP 1245, 1994, p. 1.

[3] R.N. Singh, R. Kishore, S. Mukherjee, P.K. De, S. Banerjee, in: Proceedings of 2nd International Workshop on 'Interaction of Hydrogen Isotopes with Structural Materials – IHISM-04' workshop held at Sarov, Russia from April 12–17, 2004.

[4] Kakrapar Atomic Power Station Safety Report: Accident Analysis Rev. 1, vol. II, Loss of Coolant Analysis (LOCA), 1996, pp 5.17–5.60 (Chapter 5.3).

[5] W. Dietz, R.W. Cahn, P. Haasen, E.J. Kramer (Eds.), Materials Science and Techno. A Comprehensive Treatment, vol. 10B Nuclear Materials, 1994, p. 53 (Chapter 8).

[6] C. Lemaignan, A.T. Motta, Materials Science and Techno. A Comprehensive Treatment vol. 10B, 1994, p. 1 (Chapter 7).

[7] C.D. Williams, React. Technol. 13 (2) (1970) 147.

[8] C.E. Coleman, B.A. Cheadle, C.D. Cann, J.R. Theaker, in: E.R. Bradley, G.P. Sabol (Eds.), Zirconium in the Nuclear Industry: 11th International Symposium, ASTM STP 1295, 1996, p. 884.

[9] E.F. Ibrahim, B.A. Cheadle, Can. Metall. Quart. 24 (3) (1985) 273.

[10] V. Perovic, G.C. Weatherly, R.G. Fleck, Can. Metall. Quart. 24 (1985) 253.

[11] B.A. Cheadle, C.E. Coleman, H. Litcht, Nucl. Technol. 57 (1982) 413.

[12] R.G. Fleck, V. Perovic, E.T.C. Ho, Ont. Hydro Res. Rev. (8) (1993) 1.

[13] D. Srivastava, G.K. Dey, S. Banerjee, Metall. Trans. 26A (1995) 2707.

[14] A. Salinas-Rodriguez, M.G. Akben, J.J. Jonas, E.F. Ibrahim, Can. Metall. Quart. 24 (1985) 259.

[15] L.G. Bell, J. Nucl. Mater. 57 (1975) 258.

[16] R.S.W. Shewfelt, Can. Metall. Quart. 23 (1984) 441.

[17] R.N. Singh, R. Kishore, T.K. Sinha, S. Banerjee, BARC Report No. BARC/2000/E/029.

[18] R.S.W. Shewfelt, L.W. Lyall, D.P. Godin, J. Nucl. Mater. 125 (1984) 228.

[19] R.N. Singh, R. Kishore, G.K. Dey, T.K. Sinha, S. Banerjee, R.V. Ramanujan (Eds.), Advances in Physical Metallurgy, Gordon and Beach Publishers, New York, 1995, p. 451.

[20] K. Kapoor, K. Muralidharan, N. Saratchandran, J. Mater. Eng. Perform. 08 (01) (1999) 61.

[21] D.L. Douglass, Atomic Energy Review (Suppl.), IAEA, Vienna, Austria, 1971.

[22] S. Banerjee, J.K. Chakravartty, J.S. Dubey, R.N. Singh, D. Srivastava, in: Proceedings of the Sypmosium Zirconium 2002 Held at Bhabha Atomic Research Centre from 11–13th September, 2002, p. 40 (Chapter I).

[23] E. Tenckhoff, in: Deformation Mechanisms, Texture and Anisotropy in Zirconium and Zircaloy, ASTM STP 966, 1988, Philadelphia.

[24] N. Saratchandran, NFC Hyderabad, personal communication.

[25] A.J. Anderson, R.B. Thompson, C.S. Cook, Metall. Mater. Trans. A 30A (1999) 1981.

[26] G.E. Dieter, Mechanical Metallurgy, SI Ed., McGraw Hill Book Company, 1988, p. 256.

[27] J.D. Baird, Metallurgical Review, vol. 149, The Metals and Metallurgical Trust, 1971, p. 1.

[28] P.G. McCormick, Acta Metall. 20 (1972) 351.

[29] R.W. Hayes, Acta Metall. 31 (3) (1983) 365.

[30] L.P. Kubin, Y. Estrin, Acta Metall. 38 (1990) 697.

[31] J.M. Robinson, M.P. Shaw, Int. Mater. Rev. 39 (1994) 113.

[32] S. Venkadesan, C. Phaniraj, P.V. Shivprasad, P. Rodriguez, Acta Metall. Mater. 40 (1992) 569.

[33] J. Weertman, J.R. Weertman, Elementary Dislocation Theory, MacMillan, London, 1964.

[34] T.H. Courtney, Mechanical Behavior of Materials, McGraw Hill, New York, 1990, p. 140.

[35] R.W. Hertzberg, Deformation and Fracture Mechanics of Engineering Materials, 2nd Ed., John Wiley, 1986, p. 154.

[36] A. Cottrell, An Introduction to Metallurgy, 2nd Ed., 1975.

[37] A.H. Cottrell, Philos. Mag. 74 (1953) 829, in relation of properties to microstructure, ASM, 1953.

[38] A.W. Sleeswyk, Acta Metall. 6 (1958) 598.

[39] A. Van Den Beukel, Phys. Status Solidi (a) 30 (1975) 197.

[40] V. Ramchandran, R.E. Reed-Hill, Metall. Trans. 1 (1970) 2105.

[41] J.H. Holloman, Trans. Am. Inst. Min. Metall. Eng. 162 (1945) 268.

[42] P. Ludwik, Elemente der Technologischem Mechanik, Julius Springer, Berlin, 1909, p. 32.

[43] H.W. Swift, J. Mech. Phys. Solids 1 (1952) 1.

[44] E. Voce, J. Inst. Met. 74 (1948) 537.

[45] M. Zhou, M.P. Clode, Mech. Mater. 27 (1998) 63.